We are IntechOpen,
the world's leading publisher of
Open Access books
Built by scientists, for scientists

4,800
Open access books available

122,000
International authors and editors

135M
Downloads

Our authors are among the

154
Countries delivered to

TOP 1%
most cited scientists

12.2%
Contributors from top 500 universities

CLARIVATE ANALYTICS
BOOK CITATION INDEX
INDEXED

WEB OF SCIENCE™

Selection of our books indexed in the Book Citation Index
in Web of Science™ Core Collection (BKCI)

Interested in publishing with us?
Contact book.department@intechopen.com

Numbers displayed above are based on latest data collected.
For more information visit www.intechopen.com

Diluted magnetic semiconductor nanocrystals in glass matrix

N. O. Dantas[1], E. S. Freitas Neto [1] and R. S. Silva [1,2]

[1]*Laboratório de Novos Materiais Isolantes e Semicondutores (LNMIS), Instituto de Física, Universidade Federal de Uberlândia, 38402-902, Uberlândia, Minas Gerais, Brazil*
[2]*Instituto de Ciências Exatas e Naturais e Educação (ICENE), Licenciatura em Física, Universidade Federal do Triângulo Mineiro, 38025-180, Uberaba, Minas Gerais, Brazil*

1. Introduction

Diluted magnetic semiconductor (DMS), are semiconductors in which a magnetic impurity is intentionally introduced; a small fraction of the native atoms in the hosting non-magnetic semiconductor material is replaced by magnetic atoms. The main characteristic of this new class of compounds is the possibility of the onset of an exchange interaction between the hosting electronic subsystem and electrons originating from the partially-filled *d* or *f* levels of the introduced magnetic atom (Erwin et al., 2005; Norris et al., 2008). Once that onset is reached in the above-mentioned exchange interaction, it enables the control of both the electronic, and the optical properties of the end material, using external fields in regimes hardly achieved with other classes of materials. Slightly transitions in metal-doped II-VI and IV-VI semiconductor, as for instance, $Cd_{1-x}Mn_xS$, $Pb_{1-x}Mn_xS$, and $Pb_{1-x}Mn_xSe$, is a typical diluted magnetic semiconductor, in which a small amount of Mn^{2+} is substitutionally incorporated into the hosting CdS, PbS and PbSe semiconductor crystal structure (Ji et al., 2003; Silva et al., 2007; Dantas et al., 2008; Dantas et al., 2009).

Quantum confinement effects can be considered with the incorporating of magnetic ions in semiconductors NCs, modifying the optical, magnetic, and electronic properties in relationship to semiconductor bulk. The transition metal ion (Mn^{2+}) d-electrons, usually located in the band gap region of the hosting semiconductor, are available to promote exchange interactions to the sp-band electrons of the hosting semiconductor (Fudyna, 1988). The sp-d exchange interaction taking place in II-VI, and IV-VI DMS (as for instance in $Cd_{1-x}Mn_xS$, $Pb_{1-x}Mn_xS$ and $Pb_{1-x}Mn_xSe$) provides a unique interplay between optical properties and magnetism, which could be strongly-dependent upon the doping mole fraction (*x*) (Silva et al., 2007; Dantas et al., 2008; Dantas et al., 2009). By varying the material's doping profile (*x*) a fine tuning of the semiconductor band gap energy can be achieved. Furthermore, quantum size effects caused by the shrinking in DMS bulk II-VI and IV-VI, as in nanosized particles, enhance the optical and the magnetic properties, even further. In addition, in the presence of applied magnetic fields the sp-d interaction involving electrons, holes, and the hosted magnetic ions is affected, as a result modifying the DMS properties and providing the material basis for new applications in magneto-optical,

magneto-transport, spintronics, lasers, and infrared devices. Theoretical models to explain the incorporation of magnetic impurities in nanocrystals are reported in the literature (Erwin et al., 2005; Dalpian & Chelikowsky, 2006; Norris et al., 2008), such as the "self-purification" mechanisms which are explained through energetic arguments. These mechanisms show that the formation energy of magnectic impurities increases when the NCs size decreases. Moreover, the binding energy of the impurities in the crystalline faces is highly dependent on the semiconductor material, such as the crystal structure, and NCs shape.

Nanocrysttaline structures doped with a small amount of magnetic impurities are obtained from a controlled process known as thermal diffusion of precursor ions, for NC formation in conditions of thermodynamic equilibrium. In this context, $Cd_{1-x}Mn_xS$, $Pb_{1-x}Mn_xS$, and $Pb_{1-x}Mn_xSe$ NCs have been synthesized by fusion method in glass matrixes. In this chapter we report the synthesis process of nanocrystals in a glass matrix, the synthesis routes of diluted magnetic semiconductor $Cd_{1-x}Mn_xS$, $Pb_{1-x}Mn_xS$, and $Pb_{1-x}Mn_xSe$ nanocrystals grown on a borosilicate glass matrix and their investigation by experimental techniques of optical absorption (OA), photoluminescence (PL), electron paramagnetic resonance (EPR) spectra, atomic force microscope (AFM), and x-ray diffraction (XRD).

2. Synthesis of nanocrystals in glass

Nowadays, one of the biggest interests is the nanostructured systems production which present desired physical properties to technological applications, and that are of low cost. Among the materials, which satisfy these necessities, there are nanocrystal-doped glasses (Woggon, 1997; Gaponenko, 1998). These are interesting in the physical property studies of low-dimensionally structures, and its optical transitions of electrons in quantum confinement regime (Bányai & Koch, 1993; Woggon, 1997; Gaponenko, 1998). Since the origin of nanocrystal-doped glasses, the optical fiber-based communication systems, which before had the entire amplifying process and optical signal processing performed in an electronically way, begin to amplify and process the optical signals through the use of fully optical devices, in which the use of those devices considerably enhance the quality in signal transmission. The first evidences of nanocrystals existence in glasses undergone through thermal annealing were given by Rocksby at about 1930's (Woggon, 1997). Since the second half of 20th century, companies like Corning Glass Industries, Schott Optical Glass, Hoya, and Toshiba, have been using quantum dot-doped glasses (Gaponenko, 1998). Although, the semiconductor-doped glasses potential to application in optical devices still be a well discussed subject in diverse papers, the research continues focused in the direction of a more primary stage, where the main objective is the understanding of physics involved in this kind of material.

2.1. Nanocrystals' growth kinetics

The semiconductor nanocrystals' growth kinetics in doped glass matrixes is the resulted precipitation in a supersaturated solid solution by dopers, controlled by the diffusion process of the solved semiconductor materials in the glass matrix (Woggon, 1997; Gaponenko, 1998). The solid solution is defined as been constituted by a unique phase in which more than one atomic specie is inserted, and for which the atom identity, that occupy one or more sites, in the solution is variable (Zarzycki, 1991). In this solid solution, the

precursor elements in the glass matrix, which can move, themselves by diffusion, are considered the solutes the glass matrixes are the solvents while the quantum dots are the solid phase or the precipitated from the process. For an occurrence of precipitation, the solution must be supersaturated, i. e., the solute concentration must exceed the saturation value at a given temperature and pressure. The appearing of a new phase happens by the discreet particles formation with well-defined, well-arranged interfaces, in an aleatory way, within the original phase.

These growth kinetic processes, in general, can be divided in three different stages: the nucleation, the normal growth, and the coalescence or competitive growth (Zarzycki, 1991; Gaponenko, 1998).

2.1.1. Nucleation

In the temperature, where there is an appreciable atomic mobility, there is also a continuum rearrangement of atoms in thermal disturbance. If the phase is thermodynamically unstable, these rearrangement domains have a temporary existence, so then they are destroyed, and replaced by others. When the phase is metastable, such fluctuations are potential sources of a stable phase, and don't become permanent. The fluctuation effects can produce dots that are different in size, shape, structure, or composition.

In the simplest classical model, which was proposed by Volmer and Weber (Volmer & Weber, 1926), and Becker and Döring (Becker & Döring, 2006), it is assumed that embryos of the processes have uniform structure, composition, and identical properties to those of future phase, and only differ in shape and size. The shape, in question, is the one that results from the minimum free energy formation, which will be connected to the interface nature. If it is assumed that, in first approximation, the surface energy is independent of crystallography orientation, and the elastic deformation energy is negligible, the embryos will have a spherical shape. The embryos' size is dependent of the thermodynamic stability condition. When two phases coexist in different homogeneous regions, a phase transition or formation of a different phase within another can occur. "Nucleation", is the process of forming a new phase within an existing phase, separated by a well-defined surface.

In a supersaturated solid solution there is an excess of solute in the solvent (the solute concentration exceeds the saturation value at a given temperature and pressure). This excess can be turned into a precipitate, if the nucleation process happens. The quantum dots-doped glasses are examples of materials created by nucleation in a supersaturated solid solution, where there is the coexistence of phases: the solvent (glass matrix), the solute (doper), and the precipitate (quantum dots).

Assuming that within a determined volume (matrix) a coexistence of disperse atoms (solvent) with particles forming atoms (doper) occur, and defining g^m as a free energy per disperse atom, and g^c as the free energy per crystal atom, it is obtained that the free energy of the compound of particles varies from an amount ΔG, when the quantum dot nuclei are formed. This variation can be given by:

$$\Delta G = \Delta G' = \left(\frac{4\pi R^3}{3} \right)\left(\frac{g^c - g^m}{V} \right) + 4\pi R^2 \gamma \tag{1}$$

The term (g^c-g^m/V) of the Eq. (1), represents the free energy variation per unit of volume, R is the radius of quantum dot nucleus, V is the volume per particle in the quantum dots, γ is the surface energy per area unit.

When the matrix is supersaturated by dopers which will form the semiconductor crystalline phase, the first term of the Eq. (1) is negative, while, the second one is positive. As the terms are proportional to R^3 and R^2, respectively, it can be concluded that the second term influence will be lower when R increases and the curve ΔG versus R will increase until it reaches a maximum value and after it will decrease, as it is represented in Fig. 1.
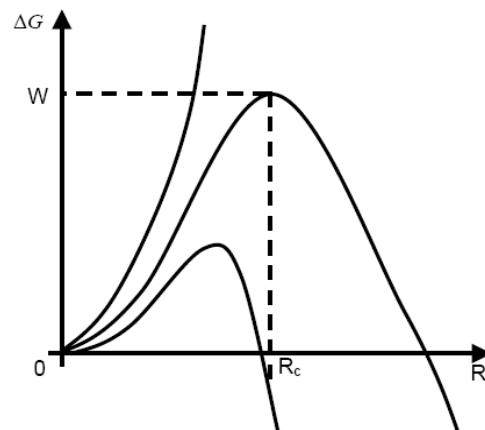
Fig. 1. Free energy variation ΔG as a function of the particle radius (R) (Christian, 1965).

The position of this maximum is given by:

$$\frac{\partial \Delta G^{`}}{\partial R} = 0 \tag{2}$$

what leads to a critical radius R_c of the quantum dot nucleus, given by:

$$R_c = \frac{2\gamma V}{(g^c - g^m)} \tag{3}$$

A particle of radius R_c will be in a instable equilibrium situation. If the radius is lower than R_c, the particle tends to be re-dissolved, once an increase in radius leads to an increase of ΔG. If the radius is greater than R_c, the particle tends to grow, once an increase in radius leads to decrease in ΔG. The particles with $R < R_c$ are called "embryos", while the ones with $R > R_c$ are called "nuclei".

The free energy variation, in a transformation, also depends on quantum dot size, which are formed in the semiconductor phase. The quantum dot radius depends on the number of particles that are dispersed in the glass matrix, and also on equilibrium concentration for the semiconductor phase. Therefore, from Gibss-Thomson's equation, the free energies can be related to semiconductor concentration in the glass matrix, as follows:

$$\left(g^m - g^c\right) = KT \ln\left[N(R)/N(\infty)\right] \tag{4}$$

Here, *N(R)* is the equilibrium concentration for the semiconductor species in quantum dots with radius *R*, *N(∞)* is the equilibrium concentration for the semiconductor species that are dispersed in the glass matrix, *K* is the Boltzmann constant, and *T* is the temperature.
The critical radius (R_c) for any volume, in terms of this equation, is expressed by:

$$R_c = \frac{2\gamma V}{KT \ln[N(R)/N(\infty)]} \tag{5}$$

which results in:

$$N(R) = N(\infty) \exp\left(\frac{2\gamma V}{KTR_c}\right) \tag{6}$$

According to Eq. (6), it is possible to determine the equilibrium concentration for quantum dots of radius *R*. In the equilibrium, the quantum dots should not increase or decrease in size, i. e., the absorbed species rate must be equal to released species rate. In Fig. 2 is presented a typical curve of these concentrations.
It is observed, in Fig. 2, that the point, where the curve intercepts the line of doping concentration existing in the matrix, and this point defines the critical radius, from which the quantum dot nuclei will grow. It is also observed that the quantum dots are completely re-dissolved when the temperature is increased from T_2 to T_3. In this case, the dissolution rate is proportional to the difference between the equilibrium concentration and the existing concentration in matrix.
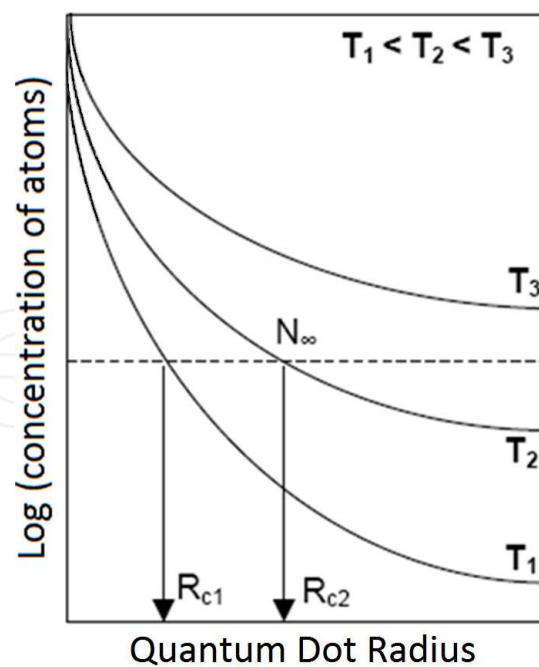

Fig. 2. The equilibrium concentration of the atoms dispersed in the matrix as a function of the quantum dot radius for three different temperatures (Barbosa et al., 1997).

Thus, the quantum dots with smaller radii will be re-dissolved much faster than those with larger radii, which would lead to their size dispersion. It is clear that, when $N(R)$ is below of $N(\infty)$, there will be no growth of any quantum dot nucleus. The ratio between $N(R)$ and $N(\infty)$ is used as a supersaturation measure, given by:

$$\Delta = \frac{N(R)}{N(\infty)} \qquad (7)$$

A matrix always will be supersaturated when $\Delta > 1$. In terms of supersaturation, the critical radius can be written as:

$$R_c = \frac{2\gamma V}{kT \ln(\Delta)} \qquad (8)$$

The supersaturation degree is also defined as follows:

$$\Delta_m = \frac{[N(R) - N(\infty)]}{N(\infty)} = \Delta - 1 \qquad (9)$$

2.1.2. Growth

The theoretical considerations, on crystals growth description, are based on three general models, on the type of liquid-crystal interface and the nature of active sites for crystallization (Zarzycki, 1991): normal growth (or continuum growth); growth determined by processes of bi-dimensional nuclei formation and subsequent increase; and coalescence or competitive growth. For briefly, it will be considered just the first, and last mechanism.

2.1.2.1. Normal growth

With the decrease in solution supersaturation during the initial stages of nucleation, the so called normal growth process starts. During this process, the nuclei that reached a critical radius increases in size, while the others are re-dissolved in the matrix (Zarzycki, 1991).

2.1.2.2. Coalescence or competitive growth

When the supersaturation degree of the matrix decreases a lot, i. e., almost all semiconductor material is already incorporated in a nucleus, the stage denominated as coalescence or competitive growth takes place. There is a competition in which the larger nanocrystals grow from the smaller ones. The study of this process is known as Coarsening Theory of Lifshitz-Slyozov, and leads to a size distribution with same name (Zarzycki, 1991 ; Gaponenko, 1998). This distribution has the peculiarity of being asymmetric around its average values, with an sudden cut to the particles with larger size, and a huge dispersion to the smaller ones. In practice, these different stages occur simultaneously in the real growth process, however, it is possible to consider each stage separately for theoretical purposes.

2.2. Diluted magnetic semiconductor nanocrystals formation: magnetic impurities incorporation

A study of Mn incorporation in semiconductors II-VI and IV-VI was performed, assuming that the adsorption of this magnetic ion occurs on surface of the three crystallography faces ((1 1 1), (1 1 0), and (0 0 1)) of these semiconductors. The obtained results, from the density functional theory, show that the binding energy of Mn, on surface of the crystallography faces, is dependent of the crystalline structure of the semiconductor materials. For crystalline structures of *zinc-blend* type (ZnS, CdS, ZnSe, and CdSe), the binding energy is in the range of 2 to 7 eV. While, for the crystalline structures of *rock-salt* type (PbS, and PbSe), this energy is around of 2 eV (Erwin et al., 2005).

The magnetic impurities incorporation in nanocrystals, produces changes in optical, magnetic, and structural properties of these materials (Furdyna, 1988; Bacher et al., 2005). The exchange interactions, between the levels sp of atoms in semiconductor nanocrystals and the level d of Mn^{2+} ions, completely modify these nanocrystals properties. Most of the semiconductor nanocrystals have a diamagnetic phase. However, with the magnetic impurities incorporation, forming a diluted magnetic semiconductor, this material starts to present paramagnetic, ferromagnetic, anti-ferromagnetic, or spin glass phases, even more, they modify the lattice parameter of semiconductor nanocrystals, and Mn-Mn exchange interactions in closer Mn ions also occur.

The electronic configuration on Mn ions introduced in diluted magnetic semiconductor is A-$(3d^5)$ or A_o $(3d^5 + h$ (holes)) (A- is the negatively charged c, and A_o denotes the neutral center). Studies show that there are three types of Mn centers, when it is incorporated to semiconductor materials. The first is formed to the Manganese in Mn^{3+} state, which is found in $3d^4$ electronic configuration with the spin in ground state S = 2, considered as a neutral accepter center A_o $(3d^4)$. The second type of center occurs when the Manganese, in Mn^{3+} state, imprisons an electron and strongly bind it to the d layer, where it starts to show an electronic configuration $3d^5$ with S = 5/2, denoted by A-$(3d^5)$. This second type of Mn center become negatively charged, been able to attract and weakly bind a hole, forming a third center , denoted by A_0 $(3d^5 + h)$ (Sapega et al., 2002).

2.3. Synthesis of DMS NCs in a glass matrix

In this section, we describe the main synthesis of DMS NCs in glasses, methods which have been being developed in recent years, by our research group. From the adequate composition, the masses of powder compounds, that will form the glass matrix as well as the DMS NCs, are measured, mixed, and homogenized.

The first step of sample preparation consisted of melting powder mixtures in an alumina crucible at high temperature for a determined time. In the sequence, a quick cooling to room temperature was undergone to the crucible containing the melted mixture. In the second step, was carried out a thermal annealing of the previously melted glass matrix at specific temperature for several hours aiming to enhance the diffusion of precursor ions into the host matrix.

The DMS NCs, which were synthesized by this methodology, growth kinetics can be explained based on the described models in sections 2.1 and 2.2. The optical, magnetic, and structural properties of these DMS NCs will be presented in the following sections.

2.3.1. Synthesis of Pb$_{1-x}$Mn$_x$S NCs

Pb$_{1-x}$Mn$_x$S NCs embedded in an oxide glass matrix were synthesized by the fusion method. The synthesis process proceeds as follows. First, the Mn-doped SiO$_2$–Na$_2$CO$_3$–Al$_2$O$_3$–PbO$_2$–B$_2$O$_3$+S (wt %) powder was melted in an alumina crucible at 1200°C for 30 min. Then, it was cooled down to room temperature. After that, thermal annealing treatment proceeded at 500°C. Finally, spherically shaped Pb$_{1-x}$Mn$_x$S NCs were formed in the glass matrix. In order to study the effects of the synthetic process on the magnetic properties of DMS NCs, four Pb$_{1-x}$Mn$_x$S samples with x-concentration varying from 0% until 40% denominated as SNABP: Pb$_{1-x}$Mn$_x$S, have been synthesized under different thermal treatments, with annealing times of 2, 4, 8, and 10 h, respectively (Silva et al., 2007).

2.3.2. Synthesis of Pb$_{1-x}$Mn$_x$Se NCs

The semimagnetic Pb$_{1-x}$Mn$_x$Se samples were synthesized in glass matrix SNABP with nominal compositions 40SiO$_2$ · 30Na$_2$CO$_3$ · 1Al$_2$O$_3$ · 25B$_2$O$_3$ · 4PbO (mol %) adding 2Se (wt %), in which the incorporation of Mn^{2+} ions varies between $0 < x < 5\%$. The preparation process consisted of melting the powder mixtures in an alumina crucible at 1200°C for 30 min. In the sequence, the crucible containing the melted mixture underwent quick cooling to room temperature. In a second step, thermal annealing of this melted and cooled glass matrix was carried out at 500°C for several hours, in order to enhance the diffusion of Pb^{2+}, Mn^{2+}, and Se^{2-} species into the host matrix, or produce a rearrangement of ions entering the formation of the NCs. This annealing process produces good quality Pb$_{1-x}$Mn$_x$Se NCs showing small size distribution of dots. The same process holds for undoped PbSe quantum dot formation. Two types of Mn-doped samples were grown: (i) SNABP matrix only doped with x-content of Mn, and labeled SNABP: xMn; (ii) SNABP templates, labeled SNABP: Pb$_{1-x}$Mn$_x$Se containing Pb$_{1-x}$Mn$_x$Se NCs with the percentage of manganese-to-lead in the range $0 < x < 5\%$ (Dantas et al., 2009).

2.3.3. Synthesis of Cd$_{1-x}$Mn$_x$S NCs

Cd$_{1-x}$Mn$_x$S NCs were synthesized in a glass matrix SNAB with a nominal composition of 40SiO$_2$ · 30Na$_2$CO$_3$ · 1Al$_2$O$_3$ · 29B$_2$O$_3$ (mol %) adding 2(CdO+S) (wt %), and Mn-doping concentration (x) varying with respect to Cd-content from 0% to 10%. The first step of sample preparation consisted of melting powder mixtures in an alumina crucible at 1200°C for 30 min. Then, the crucible containing the melted mixture underwent quick cooling to room temperature. In the second step, thermal annealing of the previously melted glass matrix was carried out at 560°C for 10 hours in order to enhance the diffusion of Cd^{2+}, Mn^{2+}, and S^{2-} species into the host matrix. As a result of the thermal annealing, Cd$_{1-x}$Mn$_x$S NCs were formed in the glass template. There were two classes of samples for different Mn concentrations: (i) doped with Mn and denominated SNAB: xMn and (ii) NC samples Cd$_{1-x}$Mn$_x$S NCs were denominated SNAB: Cd$_{1-x}$Mn$_x$S (Dantas et al., 2008).

3. Optical Properties of DMS NCs

The optical properties with the Mn^{2+} ions incorporation in Pb$_{1-x}$Mn$_x$S, Pb$_{1-x}$Mn$_x$Se, and Cd$_{1-x}$Mn$_x$S NCs, which were grown in glass matrixes through the methodologies described in section 2.3, were investigated by Optical Absorption (OA), and/or Photoluminescence spectroscopy techniques. The obtained results will be presented and discussed as follows.

3.1. Optical Absorption (OA) of Pb$_{1-x}$Mn$_x$S NCs

The optical absorption spectra of samples SNABP: Pb$_{1-x}$Mn$_x$S (x = 0, 0.003, 0.005, and 0.010) are shown in Fig. 3. Strong blue shift with respect to the optical absorption of bulk PbS (band gap at 0.28 eV) is clearly observed (see Fig. 3) in all SNABP: Pb$_{1-x}$Mn$_x$S samples, indicating the quantum confinement effect of carriers within the as-produced PbS NCs.
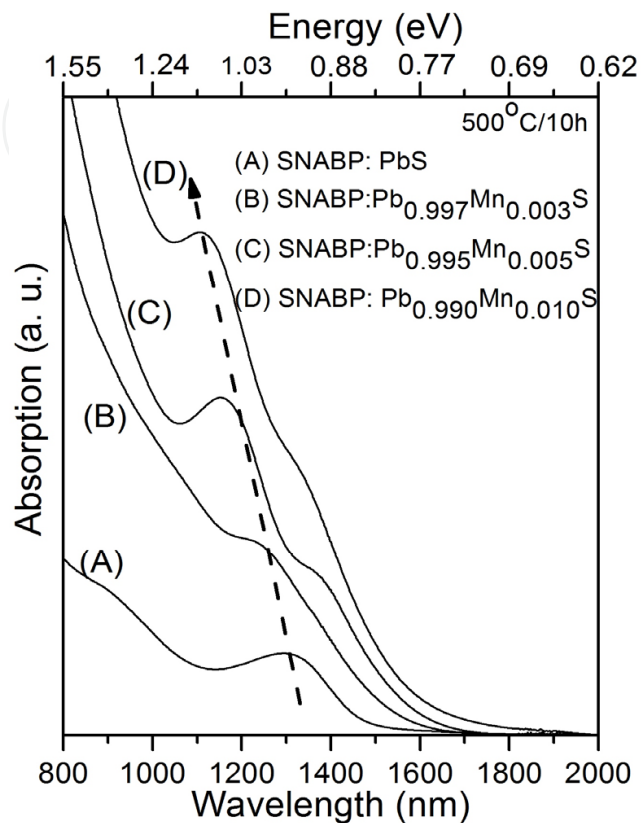

Fig. 3. Room temperature optical absorption spectra of SNABP: Pb$_{1-x}$Mn$_x$S samples. (Silva, 2008)

Furthermore, with the introduction of the magnetic impurity (Mn^{2+}) in the PbS NC lattice the optical properties are completely modified due the exchange interaction (sp-d) between the electronic subsystem of the PbS NC and electrons originated from the partially-filled Mn^{2+} ions (Lee et al., 2005). This exchange interaction, scaling with the x-content, responds for the relative blue shift of the effective band gap observed in the OA spectra of samples SNABP: Pb$_{1-x}$Mn$_x$S, as shown in Fig. 3. More specifically, effective band gaps of 0.95 eV (1307 nm), 1.00 eV (1238 nm), 1.07 eV (1158 nm) and 1.12 eV (1111 nm) were observed for x-contents of 0, 0.003, 0.005 and 0.010, respectively.

3.2. Optical Absorption (OA) of Pb$_{1-x}$Mn$_x$Se NCs

Optical absorption spectra recorded for different samples have provide strong evidences of Mn^{2+} ion incorporation into the PbSe NCs samples, labeled as SNABP: Pb$_{1-x}$Mn$_x$Se ($x>0$). Due to the exchange interaction (**sp-d** hybridization) between electronic subsystems, the incorporation of magnetic ion in NCs modify the confined electronic states and thus, the optical properties of the quantum dots (Furdyna, 1988; Ohno, 1998). This exchange

interactions causes the blue shift of optical resonance, proportional to the Mn-concentration x, between $Pb_{1-x}Mn_xSe$ and PbSe NCs.

Figure 4 shows this effect for SNABP: $Pb_{1-x}Mn_xSe$ samples embedded with $Pb_{1-x}Mn_xSe$ with x = 0, 0.005, 0.01 and 0.05%. The observed NC blue shift changes from 0.84 eV (1476 nm) for x=0 to 0.89 eV (1398 nm) for x = 0.05%. Effects associated to the spatial confinement can be estimate since bulk semiconductor lead-salt $Pb_{1-x}Mn_xSe$ samples have rock salt crystal structure with a direct band-gap, at the **L**-point of the Brillouin zone, with a value ranging between 0.28 eV, for bulk PbSe, and 3.4 eV, for the bulk MnSe which displays hexagonal structure. The appearance of well defined subband peaks in the absorption spectra demonstrates a relatively small size distribution and good quality of these SNABP: $Pb_{1-x}Mn_xSe$ samples synthesized by fusion method. The absorption peak observed near 570 nm, for SNABP: xMn sample, is attributed to the presence of 0.05% of Mn^{2+} ion.
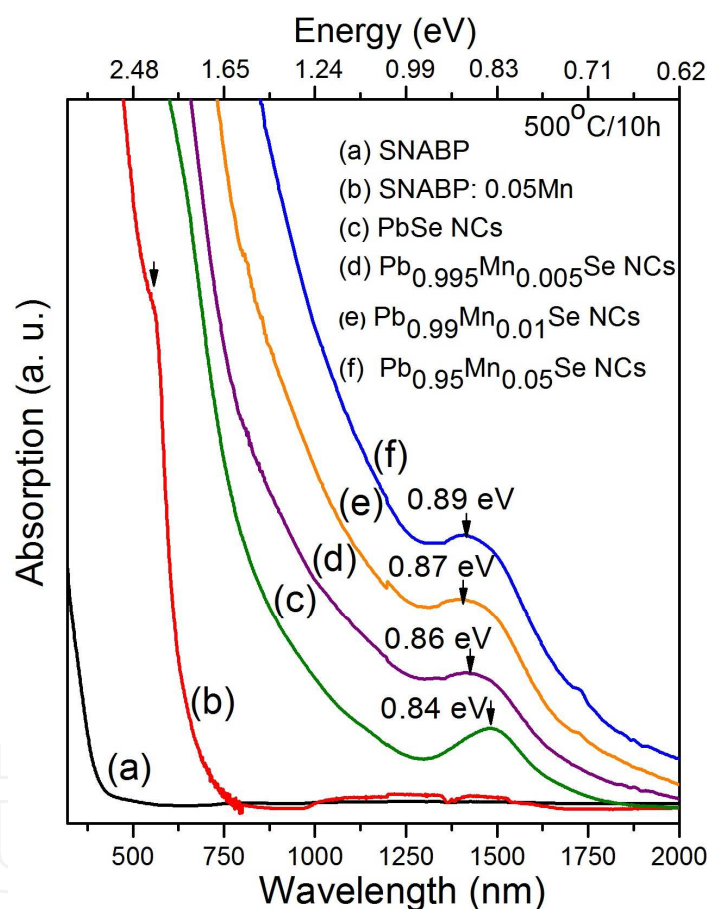
Fig. 4. Room temperature optical absorption spectrum as a function of the wavelength: for a (a) glass matrix; (b) for glass matrix doped with x = 0.05% Mn (SNABP: xMn) and $Pb_{1-x}Mn_xSe$ NCs (SNABP: $Pb_{1-x}Mn_xSe$) for Mn-concentration: (c) x = 0; (d) x = 0.005%; (e) x = 0.01%; and (f) x = 0.05%. (Dantas et al., 2009)

Atomic force microscopy (AFM) images of these samples (shown in section 5.2) confirm the same average size for both the PbSe NCs and $Pb_{1-x}Mn_xSe$ NCs. Then, this blue shift in the OA spectra (Fig. 4), between PbSe and $Pb_{0.95}Mn_{0.05}Se$ NCs, was associated to the incorporation of Mn^{2+} ions in the PbSe dot structure.

3.3. Optical Absorption (OA) of Cd$_{1-x}$Mn$_x$S NCs

The OA spectra of the Cd$_{1-x}$Mn$_x$S NC samples, that were synthesized as described in section 2.3.3, were obtained using a spectrophotometer Varian-500 operating between 175–3300 nm. OA spectra provided other evidence of Mn^{2+} ion incorporation in the SNAB: Cd$_{1-x}$Mn$_x$S and SNAB: xMn samples.(Wang et al., 2004; Levyayb et al., 1998) The introduction of magnetic impurities in semiconductors modified NCs' optical properties as a result of *sp-d* exchange interactions between electrons confined in dot states and located in the partially filled Mn^{2+} states, causing a blue shift with increasing x in the band gap of Cd$_{1-x}$Mn$_x$S samples compared to undoped CdS NCs.
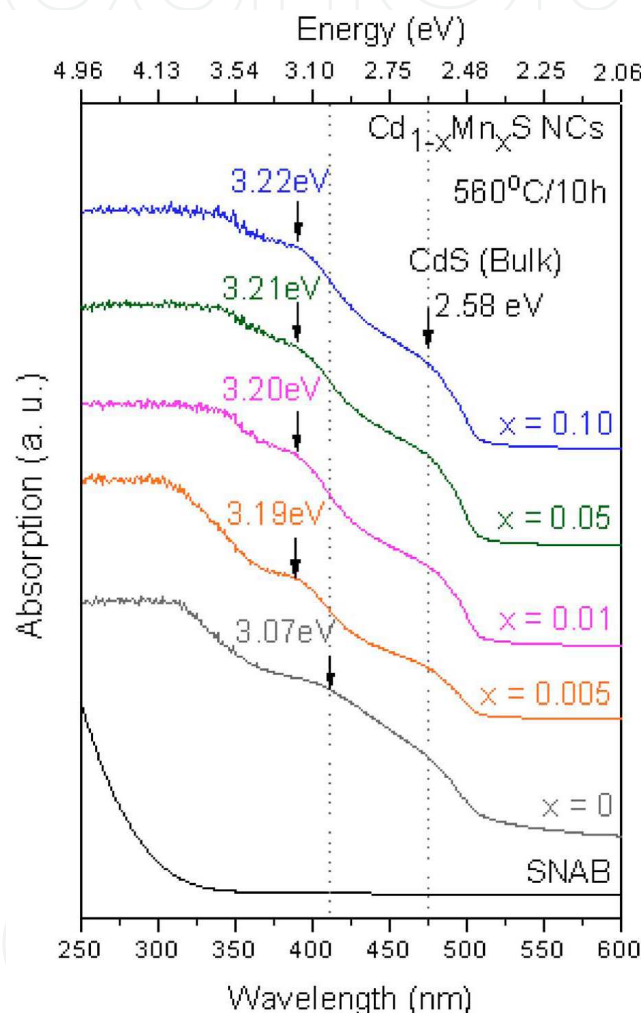
Fig. 5. OA spectra of Cd$_{1-x}$Mn$_x$S NCs embedded in a glass matrix for samples with concentrations: x = 0, 0.005, 0.01, 0.05, and 0.10. The blue shift is marked by lines and arrows. (Dantas et al., 2008)

Figure 5 shows this effect in embedded Cd$_{1-x}$Mn$_x$S NCs samples, for x=0, 0.005, 0.01, 0.05, and 0.10. Note the blue shift of band gap varying from 3.07 eV (403 nm) to 3.22 eV (385 nm). The band gap of Cd$_{1-x}$Mn$_x$S semiconductor varies between 2.58 eV (CdS bulk) and 3.5 eV (MnS bulk). The appearance of well defined subband peaks in the absorption spectrum demonstrates the high quality of the synthesized samples and the relatively small distribution of the NCs.

Using a simple confinement model based on effective-mass approximation (Brus, 1984), the energy of the lowest exciton state in the microcrystallites of radius R smaller than the exciton Bohr radius a_B can be estimated by the following expression: $E_{conf} = E_g + \left(h^2\pi^2/2\mu R^2\right) - 1.8\left(e^2/\varepsilon R\right)$, where E_g is the energy gap of material (bulk), μ the reduced effective mass; e the elementary charge, ε the dielectric constant, and the estimated average radius for CdS NCs was R ~ 2.2 nm.

As all samples were subjected to the same thermal annealing at 560°C for 10 hours, is expected that the $Cd_{1-x}Mn_xS$ NCs have the same size as the corresponding CdS NCs, in agreement with AFM data which will be shown in section 5.3. Therefore, the OA resonance blue shift that was observed in Fig. 5, which increases with increasing Mn^{2+} concentration, occurred due to the incorporation of Mn^{2+} ions into CdS NCs.

3.4. Photoluminescence (PL) of $Cd_{1-x}Mn_xS$ NCs

Through the OA spectra, shown in Fig. 5 (section 3.3), we have confirmed that there was the formation of $Cd_{1-x}Mn_xS$ NCs with quantum confinement properties as well as bulk-like properties. The formation of these NCs can also occur, even in the quick cooling, for unannealed samples, which we shall call of $Cd_{1-x}MnS$ NCs as-grown samples. The room temperature PL spectra of the $Cd_{1-x}Mn_xS$ NCs as-grown samples were acquired with a spectrofluorometer (NanoLog – Horiba JY).

Figure 6(a) shows the PL spectra at room temperature of $Cd_{1-x}Mn_xS$ NCs as-grown samples with different nominal x-concentrations: 0, 0.005, 0.050, and 0.100. The samples were excited at the absorption band edge of the NCs with bulk-like properties (510 nm), which implies that the electrons are occupying the bottom of conduction band (CB).

Our results clearly indicate that nonradiative decay paths are present, alongside the radiative recombination of the electron-hole pairs (E_{e-h}), which implies that the energy levels Mn^{2+} ($^4T_1$), trap (1), and trap (2) are occupied by electrons. The recombination aspects are well described in the diagram depicted in Fig. 6(b) which shows the emission I between the levels $^4T_1$ and $^6A_1$, characteristic of the d orbital of Mn^{2+} ion when it is substitutionally incorporated in semiconductors II-VI (Zhou et al., 2006; Beaulac et al., 2008; Archer et al., 2007). In these materials the Mn^{2+} ions can be substitutionally incorporated in two distinct sites: one in the NC-core (labeled as S_I), and other near the NC-surface (labeled as S_{II}).

The traps (1) and (2) are deep defect levels attributed to the CdS (Smyntyna et al., 2007), whose origins are not quite clear until the moment. Despite of its not so clear origin, we assume that, these two defect levels are possibility related to the V_{Cd}-V_S divacancy centers with different orientations, in analogy to the studies performed for CdSe NCs with hexagonal wurtzite structures (Babentsov et al., 2005), a material that presents great similarities with ours. It was shown that there are two energetically different divacancies: an oriented along the hexagonal c-axis (assigned to trap (1)), and other oriented along the basal Cd-Se bond directions (assigned to trap (2)). This divacancy model could also be used to explain the origins of the two deep traps (1) and (2) in CdS NCs with hexagonal wurtzite structures as well as DMS $Cd_{1-x}Mn_xS$ NCs. These considerations are quite reasonable since the wurtzite structure is a common phase for CdS NCs grown in a glass matrix (Cheng et al., 2006; Xue et al., 2009) as well as for $Cd_{1-x}Mn_xS$ NCs (0 < x ≤ 0.500) (Jain, 1991).
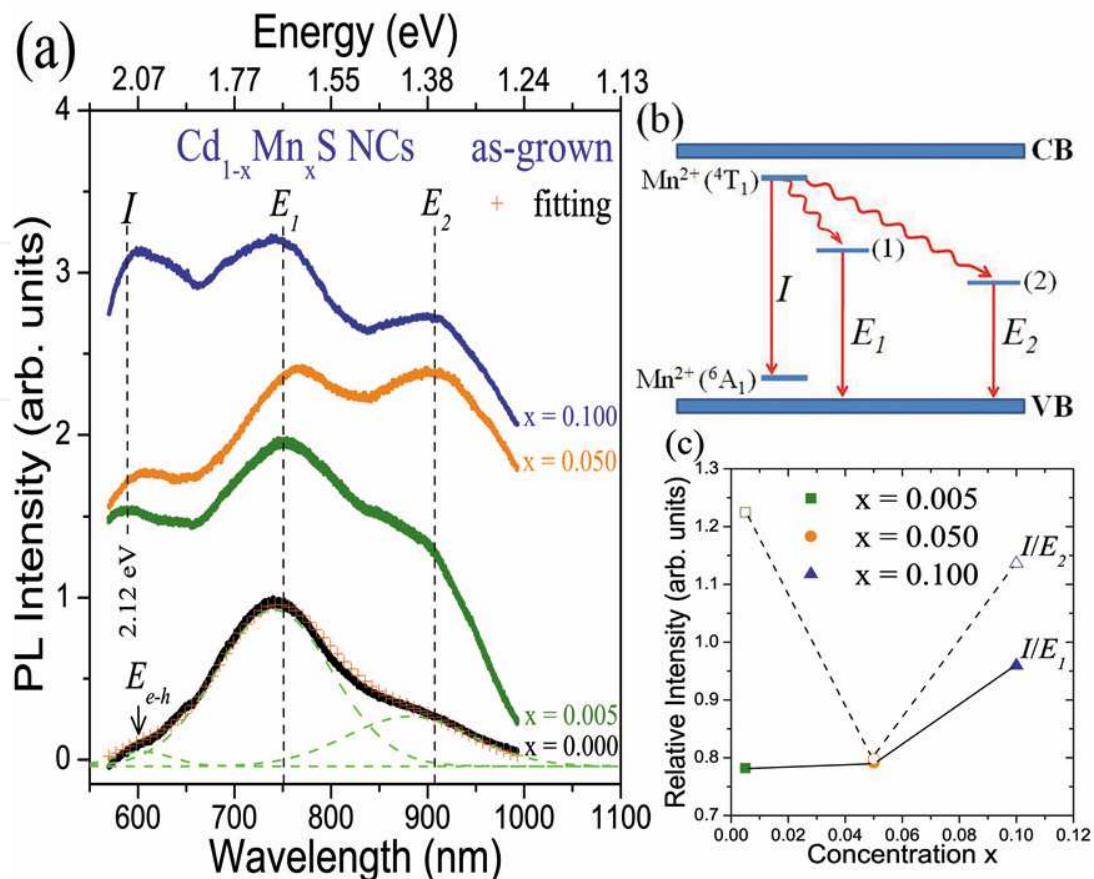
Fig. 6. (a) Room temperature PL spectra of as-grown $Cd_{1-x}Mn_xS$ NCs embedded in the glass matrix SNAB for samples with x = 0, 0.005, 0.050, and 0.100. (b) Schematic diagram showing the radiative recombinations I, E_1, and E_2 by the straightened arrows. The nonradiative transitions from the level $^4T_1$ to trap-levels (1) and (2) are represented by the wavy arrows. (c) Relative intensities between the emissions I and E_1 (solid line), and the emissions I and E_2 (dashed line).

From these two traps, there are the emissions E_1 and E_2 which can be observed in Fig. 6(a) for all samples. The PL spectra of CdS NCs (x = 0.000) were fitted using three like-gaussian components associated to these emissions (E_1 and E_2) as well as the radiative recombination of the electron-hole pairs (E_{e-h}). It is clear that the emissions E_1 and E_2 are more intense than the emission E_{e-h}, showing that the nonradiative processes are dominant from the CB bottom to trap-levels (1) and (2). Figure 6(a) also shows that an overlap, between the emissions E_{e-h} and I for the $Cd_{1-x}Mn_xS$ NCs samples with x = 0.005, 0.050, and 0.100, takes place. Undoubtedly, this overlapped band is more intense than the band of the emission E_{e-h} observed for CdS NCs samples, which indicates that majority contribution of the overlapped band can be attributed to emission of M^{2+} ion ($^4T_1 - {}^6A_1$).

Related to I emission was observed that for $Cd_{1-x}Mn_xS$ NCs grown in a colloidal solution, it is suppressed due to nonradiative processes when the Mn^{2+} ions are incorporated in the site S_{II} (Zhou et al., 2006). Thus, the strong emission I, observed in the PL spectra of the $Cd_{1-x}Mn_xS$ NCs samples (see Fig. 6(a)), gives evidence that the Mn^{2+} ions are substitutionally located in the core of nanoparticles, i.e., in the site S_I. Figure 6(c) shows the behavior of relative intensity between the emissions I and E_1 (I/E_1), and the emissions I and E_2 (I/E_2), for different x-concentration. The enhancement in relative intensity I/E_1 shows that the

increasing in x-concentration favors the incorporation of Mn^{2+} ions in the NC-core (S_I). On the other hand, the I/E_2 relative intensity curve presents a completely different shape, where a decrease in the I/E_2 is followed by an increase with the augment of x-concentration. Such kind of behavior can be understood taking into account nonradiative processes, in order that electron transfers occur from the level $^4T_1$ to the trap-levels (1) and (2), as schematically depicted in the Fig. 6(b) by the wavy arrows. The values I/E_2 are larger than I/E_1 for x = 0.005 and 0.100, indicating that, there is a smaller energy transfers (via electrons) to trap (2) than to trap (1) for these two x-concentrations. While for x = 0.050, the energy transfers from the level $^4T_1$ to the trap-levels (1) and (2) are practically equals. These results indicate that possibly there is a competition between the electron transfers for the trap-levels dependent of the x-concentration.

4. Magnetic properties of DMS NCs

The physical properties of semiconductor nanocrystals change with the incorporation of magnetic impurities, making them diluted magnetic semiconductors. This phenomenon occurs due to the sp-d exchange interaction, which involves Mn ions and electrons in conduction band or holes in the valence band, when there are Mn-doped semiconductors II-VI or IV-VI. This exchange interaction causes changes in the magnetic properties of the nanocrystals, influencing the sp-d exchange interactions of these materials.

4.1. Electron Paramagnetic Resonance (EPR)

A study of the Manganese's magnetic properties in host matrixes can be performed from the EPR technique. The studies by this technique, to the obtained results, confirm that the oxidation state of Mn is 2+, in which the Mn^{2+} ions belong to the group 3d. The free ions of this group present, in their ground configuration, the 3d incomplete layer, which is responsible for the paramagnetism. In the presence of a crystalline lattice, the Mn^{2+} ions start to have the splitted by the crystalline field. This splitting produces a reduction in the orbital movement contribution of the magnetic moment, been the magnetism from these ions fundamentally attributed to the electronic spin (Silva, 2008).

The crystal structure of the hosting semiconductor has a strong influence into the incorporated Mn^{2+}-ions, as observed in the EPR spectrum recorded from the glass sample embedded with $Pb_{1-x}Mn_xS$, $Pb_{1-x}Mn_xSe$, and $Cd_{1-x}Mn_xS$ NCs, favouring a strong electron spin-nucleus spin interaction. The experimental spectra of Mn-doped in NC samples can be modelled by the spin Hamiltonian (Dantas et al., 2008):

$$\hat{H} = \mu_e \hat{S} \cdot g_e \cdot \vec{B} + D\left[S_z^2 - S(S+1)/3 \right] + E\left(S_x^2 - S_y^2 \right) + A\hat{S} \cdot \hat{I}, \qquad (10)$$

where the first term is represent the Zeeman interaction with μ_e, g_e, and $\vec{B}$ being the Bohr magneton, the Lande factor and the applied magnetic field, respectively., in which the second and third two terms describe the zero-magnetic field fine-structure splitting due to spin-spin interaction of electrons, which is nonzero only in environments with symmetries lower than cubic, and the fourth term ($A\hat{S} \cdot \hat{I}$) is stemmed from the hyperfine interaction between electron and nuclear spins. In a magnetic field the spin degeneracy of Mn^{2+}-ions

will be lifted by the Zeeman splitting, resulting in six energy levels classified by magnetic electron spin quantum number M_S. Due to hyperfine splitting, each of these transitions will be split into six hyperfine levels characterized by the magnetic nuclear spin quantum number M_I. The main hyperfine lines in the spectra are due to allowed $M_S = \pm 1$ transitions with $\Delta M_I = 0$, whereas other lines from forbidden transitions (due to breakdown of selection rule) with nonzero ΔM_I may also be observed. Hence, the typical EPR of Mn^{2+} with electron ($S = 5/2$) and nuclear ($I = 5/2$) spins is composed of 30 lines – five fine structure transitions, each splitting into six hyperfine lines. The incorporation of metal-transition in NC sites cause changes in coordination states modifies the crystal field. These changes are analyses by EPR spectra. Typical EPR of Mn^{2+} with electron ($S = 5/2$) and nuclear ($I = 5/2$) spins is composed of 30 lines – five fine structure transitions, each splitting into six hyperfine lines. For the Mn-doped in PbS, PbSe and CdS NCs the hyperfine lines were only observed for the central $M_S = 1/2 \leftrightarrow -1/2$ transition. The location of Mn^{2+} is presented in two different sites (surface and core) in NCs can be determinate by EPR measurements. In addition, the interaction constants A, D, and E depend strongly on the characteristics of the crystal field. For instance, when a Mn^{2+} ion is located close to or on the NC surface, a large structural difference between the NC and the glass matrix results in a larger hyperfine constant A and larger D and E values. Hence the EPR spectrum varies when the local structure of Mn^{2+} ion in the NC changes (Silva et al., 2007; Dantas et al., 2008; Dantas et al, 2009).

4.1.1. EPR of Pb$_{1-x}$Mn$_x$S NCs

Figure 7 shows the EPR spectra for different Mn-concentrations in $Pb_{1-x}Mn_xS$ NCs, to the samples that were annealed at 500ºC for 10 hours. The six hyperfine transitions were observed due to the electron spin-nucleus spin interaction. The lines width comes from the sum of two contributories, $\Delta H = \Delta H_I + \Delta H_D$, where ΔH_I is the width which appears in the spectra cause intermolecular processes, and ΔH_D is the width related to "spin-spin" interaction between the first neighbours of Mn (Hinckley & Morgan, 1965). These "spin-spin" interactions are proportional to r^{-3}, where r is the average distance between the Manganese atoms (Mn-Mn). To bigger distances than 55 Å (r > 55 Å) the lines are narrow and exclusively determined by ΔH_I. In this case, the EPR spectra of Mn^{2+} ion are sixtet degenerated spin what assures the presence of six hyperfine interaction lines. On the other hand, to smaller distances than 9 Å (r < 9 Å), the six hyperfine interaction lines become wider and due to the hyperfine structure collapse, the spectra appear as a single line as observed for samples with Mn-concentration of x = 0.40. The arrow-indicated structures which appear around 345 mT, are caused by different Mn^{2+} ions localizations in PbS quantum dots (core or surface).
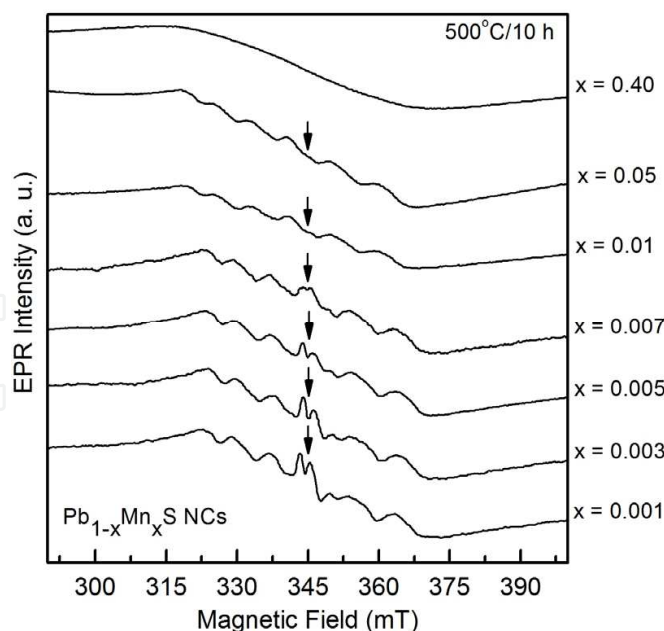
Fig. 7. EPR spectra of $Pb_{1-x}Mn_xS$ NCs for x = 0.001, 0.003, 0.005, 0.007, 0.01, 0.05, and 0.40. (Silva, 2008)

Figure 8(a) shows the EPR spectra for the SNABP: PbS, SNABP: 0.005Mn, and SNABP: $Pb_{0.995}Mn_{0.005}S$ samples, that were annealed at 500°C for 10 hours. It can be perceived that the hyperfine interactions are more clearly observed to SNABP: $Pb_{0.995}Mn_{0.005}S$ samples. These interactions, caused by the Mn^{2+} ion presence in the crystalline field from PbS quantum dots, produce a splitting in this fine structure (electronic transition $+1/2 \leftrightarrow -1/2$) into six hyperfine transitions due to electron spin-nucleus spin interaction.
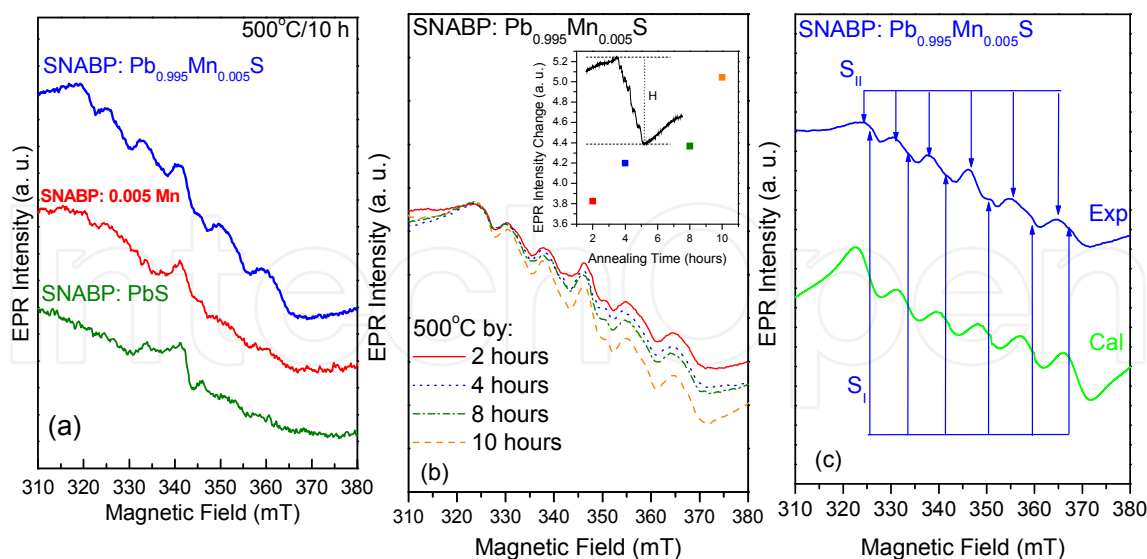
Fig. 8. (a) EPR spectra for the SNABP: PbS, SNABP: 0.005Mn e SNABP: $Pb_{0.995}Mn_{0.005}S$ samples (Silva, 2008). (b) Changing in the EPR intensity signal of the SNABP: $Pb_{0.995}Mn_{0.005}S$ sample that were annealed at 500°C by increasing times [modified from (Silva et al., 2007)]. (c) Experimental and calculated EPR spectra of $Pb_{0.995}Mn_{0.005}S$ NCs [modified from (Silva et al., 2007)].

The EPR spectra intensity modifies with the increasing in the annealing time at 500ºC, as shown in Fig. 8(b). This increasing in intensity of EPR signal is caused by a greater incorporation of Mn^{2+} ions, in PbS NCs which increase their density in the glass matrix, as observed by Atomic Force Microscopy images in Fig. 12.

For $Pb_{1-x}Mn_xS$ NCs that were grown in the glass matrix SNABP, the EPR spectra are caused by the contributions of Mn^{2+} ions incorporated in the core (Signal S_I), and/or on the surface (Signal S_{II}) of the PbS NCs. The signals S_I and S_{II} simulations was performed using the WINEPR and SINFONIA Brucker's softwares, being the resulting simulated signal compared with the obtained EPR spectrum to the SNABP: $Pb_{0,995}Mn_{0,005}S$ sample and shown in Fig. 8(c). It was observed the signal S_{II} predominance over the signal S_I, giving strong evidences of a higher Mn^{2+}-concentration near to the NC-surface. The average values obtained to hyperfine constants (A) are of A_{SI} = 8.20 mT and A_{SII} = 9.37 mT, with the electron g-factor equal to 2.005 (Silva et al., 2007). The different hyperfine constant values between the $Pb_{1-x}Mn_xS$ quantum dots and the respective bulk material, are attributed to quantum confinement of the electrons, promoting a higher interaction between the electron spin and the Mn^{2+} ion nucleus (Ji et al., 2003).

4.1.2. EPR of $Pb_{1-x}Mn_xSe$ NCs

A high sensitivity Bruker ESP-300 spectrometer, operating in the *X*-band microwave frequency (9.5 GHz), with swept static field and the usual modulation and phase sensitive detection techniques, was used to record the EPR spectra of the $Pb_{1-x}Mn_xSe$ NCs samples that were synthesized by methods described in section 2.3.
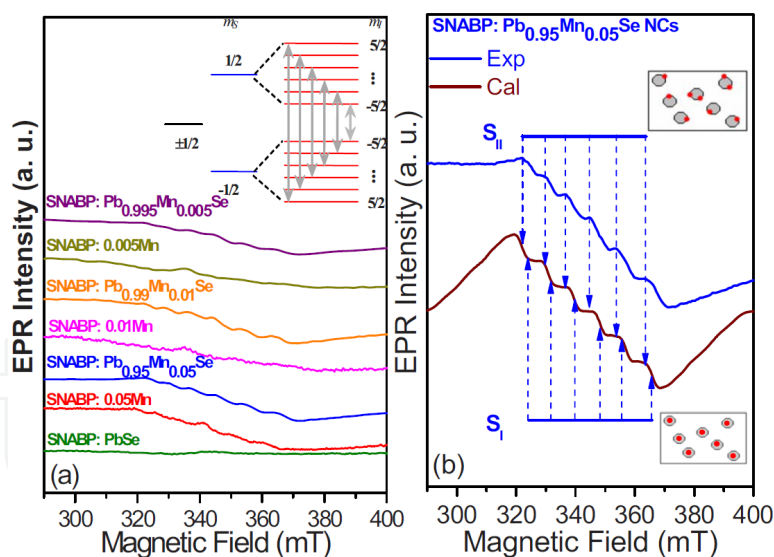

Fig. 9. Left panel: EPR spectra for pure PbSe and for semimagnetic $Pb_{1−x}Mn_xSe$ NCs, with x = 0.005, x = 0.01, and x = 0.05. In each panel, lines show the difference between undoped and doped PbSe samples. Right panel: EPR spectra of $Pb_{0.95}Mn_{0.05}Se$ NCs measured in the *X*-band and at room temperature and the computed EPR spectra obtained by a summation of two spectra with A = 7.3 mT and 7.9 mT, corresponding to Mn^{2+} sites inside labeled as S_I and on the surfaces labeled as S_{II} of NCs, for a system with S = 5/2, I = 5/2, D = 30 mT, E = 4 mT, and g = 2.005. (Dantas et al., 2009)

Figure 9(a) shows EPR spectra of a set of $Pb_{1-x}Mn_xSe$ NCs. The broad background line, in all spectra, indicates the magnetic interaction between Mn^{2+} ions inside the $Pb_{1-x}Mn_xSe$ structure.

The presence of the six hyperfine lines, as shown in the inset, confirms the uniform incorporation of Mn^{2+} ions into the dot. Figure 9(b) shows fairly good agreement between experimental (theoretical) spectrum of $Pb_{0.95}Mn_{0.05}Se$ NCs, measured in the X-band and at room temperature and shown as solid blue (dotted green) line. This EPR simulation is composed of two spectra: i) A broad line that uses a fine structure constant, $A = 7.3$ mT corresponding to Mn^{2+} ions inside the NC, ii) a stronger fine structure constant $A = 7.9$ mT corresponding to ions located close to the surface. The hyperfine parameters are $D = 30$ mT, $E = 4$ mT, and the Mn parameters are $S_{Mn} = 5/2$, $I = 5/2$, and $g_{Mn} = 2.005$.

Analysis of the EPR spectra (shown in Fig. 9) provided further evidence for the presence or absence of doped PbSe dots. The incorporation of Mn^{2+} ions in $Pb_{1-x}Mn_xSe$ NCs is confirmed by the presence of the six central hyperfine lines in the EPR spectrum. These hyperfine lines are not present in glass samples only doped with Mn^{2+} ions.

4.1.3. EPR of $Cd_{1-x}Mn_xS$ NCs

The room-temperature modifications in the electronic states induced by Mn^{2+} ion incorporation into CdS NCs (forming $Cd_{1-x}Mn_xS$ NCs) were examined by EPR using a high sensitivity Bruker ESP-300 spectrometer operating in the X-band microwave frequency (9.5 GHz).

Figure 10(a) shows EPR spectra for the synthesized sample set. The broader background signal observed in the EPR spectra is due to the spin-spin interaction between Mn^{2+} electrons when they are incorporated into the $Cd_{1-x}Mn_xS$ NCs.

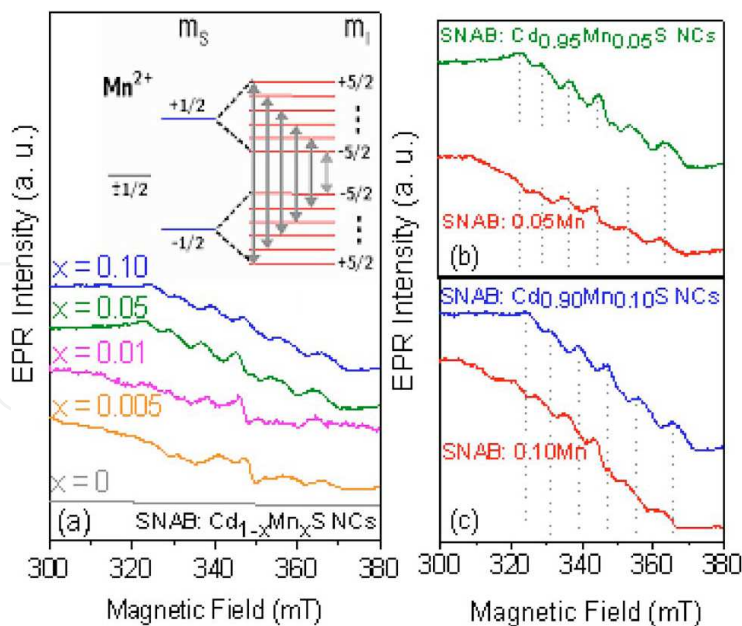Fig. 10. Panel (a) room temperature EPR spectra of $Cd_{1-x}Mn_xS$ NCs for samples with concentration: $x = 0$, 0.005, 0.01, 0.05, and 0.10. Panels (b) and (c) EPR spectra of glass matrix doped with xMn and $Cd_{1-x}Mn_xS$ NCs for $x=0.05$ and 0.10, respectively. (Dantas et al., 2008)

The six line structure confirms the uniform incorporation of Mn^{2+} ions into the host CdS NC structure, whereas the broader EPR line indicates the presence of magnetic exchange interaction when two Mn^{2+} ions get close enough and are found in small agglomerate islands. The difference between the glass samples (SNAB: xMn and SNAB: $Cd_{1-x}Mn_xS$ NCs) is observed in the EPR spectra [Figs. 10(b) and 10(c)]. Note that the hyperfine interaction due to Mn^{2+} ions results from the presence of a crystalline field in CdS NCs. The hyperfine interaction observed in the spectrum of glass samples doped with Mn^{2+} is not as evident as those observed for $Cd_{1-x}Mn_xS$ NCs. This difference could possibly be attributed to the formation of small islands of crystalline phase MnO. (Mukherjee et al., 2006)

It has already been reported that Mn^{2+} ions are incorporated into two distinct sites of NCs; when found at the dot core, it produces the EPR signal S_I, when located on or near the NCs surface it produces the EPR signal S_{II}. (Silva et al., 2007; Zhou et al., 2006) This analysis is strongly supported by good agreement between the experimental EPR spectrum and the simulated one. In Fig. 11, the EPR spectrum of $Cd_{0.95}Mn_{0.05}S$ NCs, measured in the X-band and at room temperature, is shown as a solid blue line and the calculated one as a solid green line.
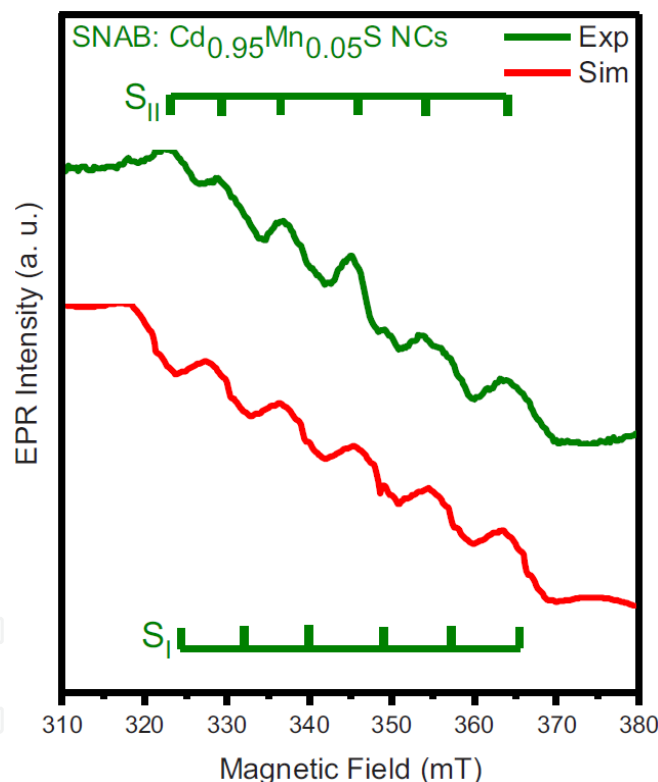
Fig. 11. Experimental and simulated EPR spectra of $Cd_{0.95}Mn_{0.05}S$ NCs. The simulation uses superposition of two spectra with A = 7.6 mT and 8.2 mT, corresponding to Mn^{2+} ions located inside (labeled as S_I) and on the surfaces (labeled as S_{II}) of NCs for a system with parameters: $S = 5/2$, $I = 5/2$, $D = 40$ mT, $E = 5$ mT, and $g_e = 2.005$. (Dantas et al., 2008)

The EPR simulation was obtained by a sum of two spectra with A = 7.6 and 8.2 mT, corresponding to Mn^{2+} ions located inside the NC (labeled as S_I) and near the NC surface (labeled as S_{II}) for a dot system with parameters: $S = 5/2$, $I = 5/2$, $D = 40$ mT, $E = 5$ mT, and $g_e = 2.005$. On the other hand, as the annealing time increases, the probability of finding

magnetic ions inside NCs occupying neighboring lattice sites as well as the number of antiferromagnetic spin correlated clusters increases. This combination of effects enhances the dipolar interaction and increases the lattice distortions on the Mn^{2+} sites. Furthermore, the accumulation of Mn^{2+} ions on the NCs surfaces also strengthens Mn–Mn interactions. (Silva et al., 2007; Zhou et al., 2006; Jian et al., 2003) As a consequence, the intensity of the broader background peak is increased.

EPR spectra provided evidence that Mn^{2+} ions are incorporated at two distinct sites: at the core and/or at the surface of CdS NCs. Influences of CdS NCs crystalline field and the presence of MnO cluster phases could be confirmed by the presence of six hyperfine lines assigned to the Mn^{2+} ions in the samples.

5. Structural properties of DMS NCs

The structural properties of the $Pb_{1-x}Mn_xS$, $Pb_{1-x}Mn_xSe$, and $Cd_{1-x}Mn_xS$ nanocrystals that were grown in glass matrixes, through the methodologies described in section 2.3, their spatial distribution, size homogeneity, and the nanocrystal shapes were analyzed by Atomic Force Microscopy using the contact mode. It was also employed the X-Ray Diffraction technique to investigate the crystalline structure of the $Pb_{1-x}Mn_xSe$ NCs samples.

5.1. Atomic Force Microscopy (AFM) of $Pb_{1-x}Mn_xS$ NCs

In the Fig. 12 are shown atomic force microscopy (AFM) images that were obtained for the SNABP: $Pb_{0.995}Mn_{0.005}S$ NCs samples, which were annealed at 500°C for 2, 4, 8, and 10 hours. It can be observed that with the increase in annealing time, the $Pb_{0.995}Mn_{0.005}S$ NCs density increases as well as their average size. The obtained values were 4.2 nm (2 hours), 4.3 nm (4 hours), 4.4 nm (8 hours), and 4.8 mn (10 hours).
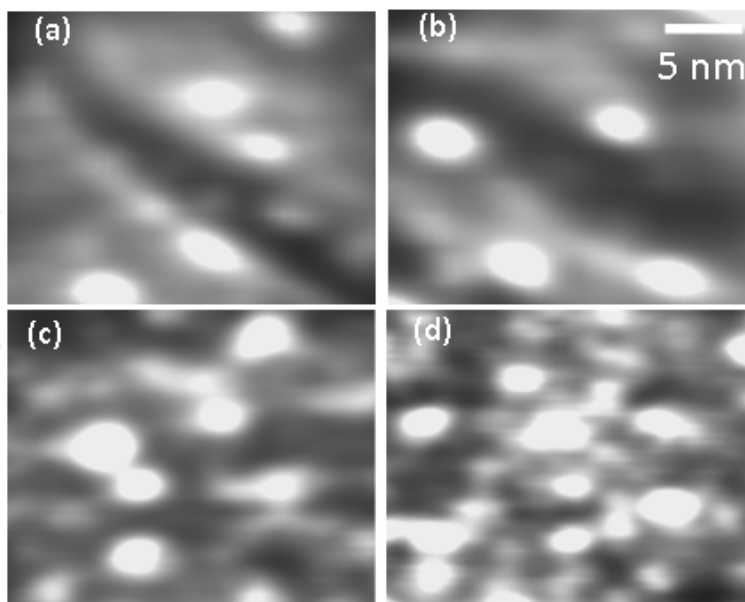

Fig. 12. AFM images of SNABP: $Pb_{0.995}Mn_{0.005}S$ NCs samples that were annealed at 500°C for (a) 2, (b) 4, (c) 8 and (10) hours (Silva, 2008).

The increase in the $Pb_{0.995}Mn_{0.005}S$ NCs density within host glass matrix results in the intensity increase of optical absorption spectra (see Fig. 3), as well as, the increase in EPR signal intensity (Fig. 8(b)).

5.2. Atomic Force Microscopy (AFM) of $Pb_{1-x}Mn_xSe$ NCs

To confirm the NCs formation on glass templates we have taken AFM images, as shown in Fig. 13, for (a) PbSe NCs and (b) $Pb_{0.95}Mn_{0.05}Se$ NCs samples. The 3D and the 2D (inset) morphologies of $Pb_{1-x}Mn_xSe$ NCs can be noted. As shown in Figures 13(a) and 13(b), is possible to estimate the average size for PbSe and $Pb_{1-x}Mn_xSe$ NCs as 5.2 nm, and with 6% the size distribution, from these AFM images.
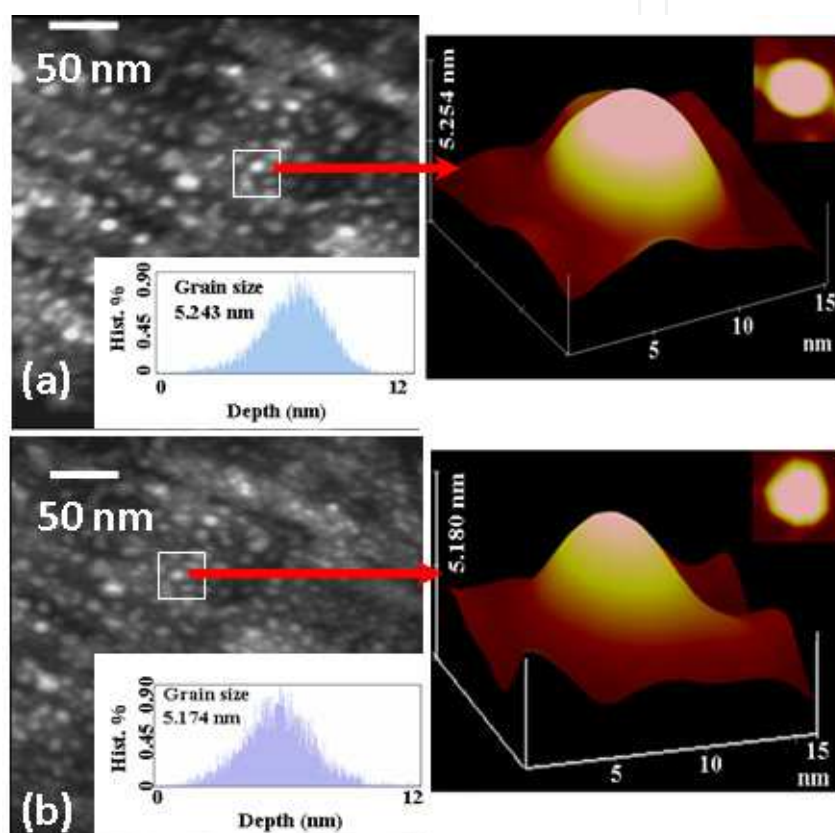
Fig. 13. AFM images of NCs showing size distribution below 6% for: (a) PbSe (b) $Pb_{0.95}Mn_{0.05}Se$. AFM image in 3D e 2D (inset) illustrates the morphology of $Pb_{1-x}Mn_xSe$ NCs, for x = 0 and 0.05. (Dantas et al., 2009)

These AFM data have confirmed that both PbSe NCs and $Pb_{1-x}Mn_xSe$ NCs have the same average size (5.2 nm). Thus, undoubtedly, the observed blue shift in OA spectra of these samples, shown in Fig. 4 (section 3.2), is related to incorporation of Mn^{2+} ions into PbSe NCs.

5.3. Atomic Force Microscopy (AFM) of $Cd_{1-x}Mn_xS$ NCs

Figure 14 shows the AFM images that were recorded for glass samples embedded with CdS NCs [Fig. 14(a)] and $Cd_{0.95}Mn_{0.05}S$ NCs [Fig. 14(b)] in order to confirm both the NCs formation and OA data for size distribution, shown in Fig. 5 (section 3.3).

The average NCs size estimated from these AFM images is at around R ~ 2.3 nm with corresponding size distributions of 5% and 9%, respectively. The AFM morphology of isolated NCs is shown in two-dimension (2D) and three-dimensions (3D) images. Thus, is observed that all samples are single-phase materials with hexagonal wurtzite structure, which is a very common phase for CdS NCs grown in glass matrix (Cheng et al., 2006; Xue et al., 2009), as well as for $Cd_{1-x}Mn_xS$ NCs $(0 < x \leq 0.500)$ (Jain, 1991).
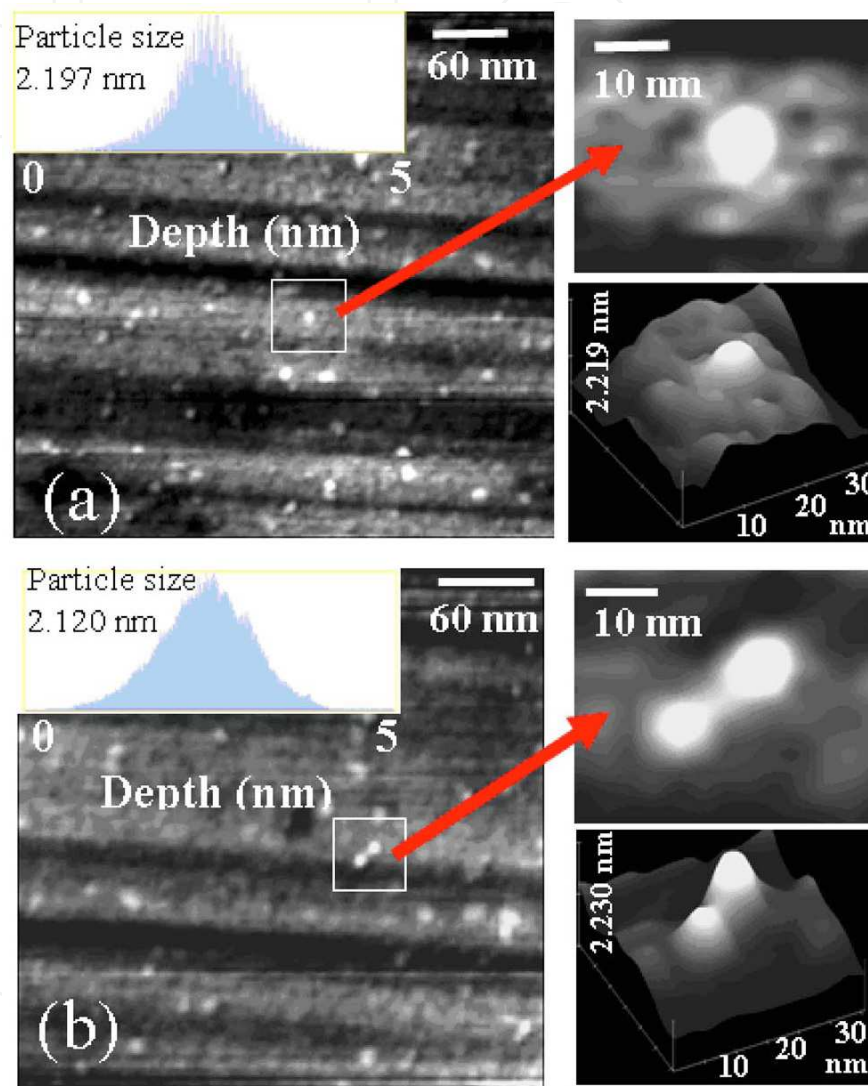
Fig. 14. AFM images showing nearly 5% size distribution and dot size R ~ 2.3 nm. The 2D and 3D images illustrate the morphology of (a) CdS NCs and (b) $Cd_{0.95}Mn_{0.05}S$ NCs. (Dantas et al., 2008)

As it was expected, the AFM data confirm that both CdS NCs and $Cd_{1-x}Mn_xS$ NCs have the same average size. Thus, it was proved that the incorporation of Mn^{2+} ions into CdS NCs provokes a blue shift in OA spectra of nanoparticles, according to the results shown in Fig. 5.

6. X-Ray Diffraction (XRD) of Pb$_{1-x}$Mn$_x$Se NCs

The XRD patterns of the SNABP: Pb$_{1-x}$Mn$_x$Se samples (x ≥ 0) for x = 0 and x = 0.05% are shown in Fig. 15(a). It is noted that the typical bulk PbSe rock salt crystal structure is preserved for the Pb$_{1-x}$Mn$_x$Se dot samples having Mn-concentration $x \leq$ 0.05%. Nevertheless, the characteristic XRD peaks is shifted towards lower diffraction angle values as the Mn^{2+} incorporation in the hosting PbSe structure increases, as shown in Fig. 15(b), and this is a clear indication that a decrease in the lattice constant is occurring. We have estimate the lattice constant (Cohen Method) of the structure using the (111), (200), and (220) peaks of the XRD spectrum. Here, the average lattice crystal constant found for Pb$_{1-x}$Mn$_x$Se samples is 6.130 Å for x = 0% (PbSe) and 6.127 Å for 0.05% incorporation of Mn^{2+} into the NCs. This monotonic decrease observed in the lattice constant can be attributed to the replacement of Pb^{2+}-ions, having larger ionic radius (119 pm) in the rock salt PbSe crystal structure, by Mn^{2+}-ions with smaller ionic radius (83 pm).
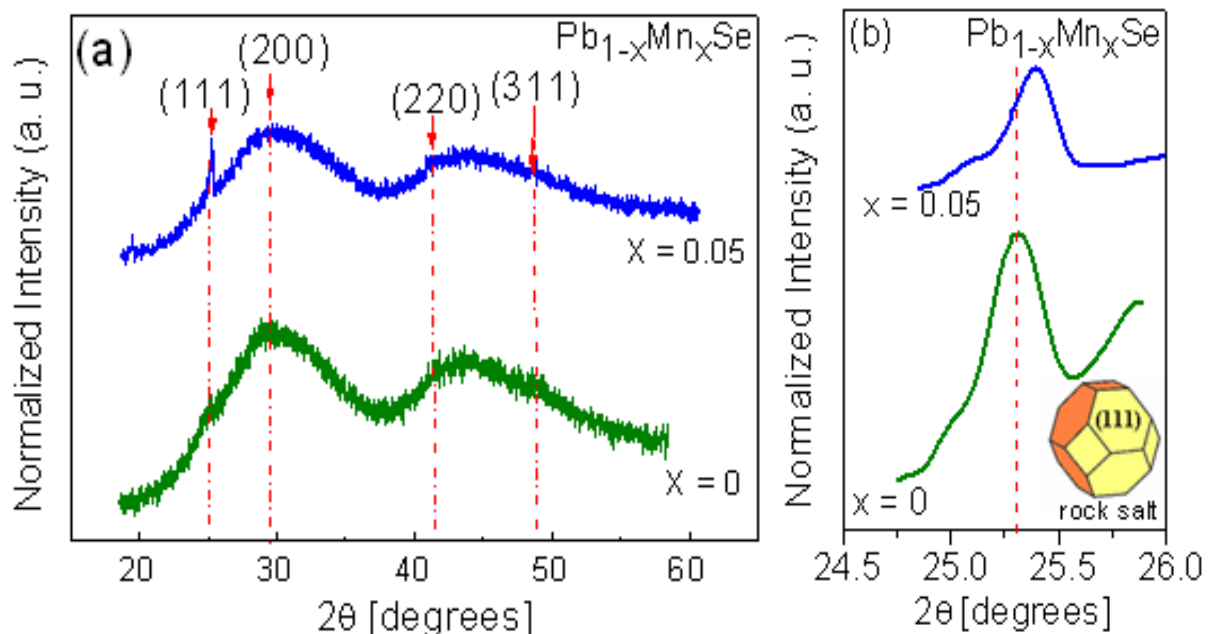
Fig. 15. (a) XRD measurements of PbSe (lower line) and Pb$_{0.95}$Mn$_{0.05}$Se (top line) NCs embedded in glass matrix. (b) The effects associated to the incorporation of Mn^{2+} ions into PbSe NCs are seen as an intensity increase (left panel) and a shift to higher 2θ diffraction angle (right panel) of the (111) peak. Probably, the diffusion is enhanced along the (111) direction. (Dantas et al., 2009)

Once the grown samples have very small Mn-concentration, the crystalline structures for undoped and doped NCs remained rock salt and showed similar values for the lattice constants. However, it is expect a decrease in the crystalline quality of samples containing higher concentration of Mn, with the possible occurrence of MnSe clusters inside the Pb$_{1-x}$Mn$_x$Se NCs.

7. Conclusions

In this chapter, it was presented the main advances, which have been obtained by us in last few years, related to study of Diluted Magnetic Semiconductor Nanocrystals (DMS NCs) in glass matrixes.

Probably the first time, $Pb_{1-x}Mn_xS$, $Pb_{1-x}Mn_xSe$, and $Cd_{1-x}Mn_xS$ DMS NCs were successfully grown in a glass matrix by the fusion method, when subjected to an adequate thermal annealing.

Our results, obtained by the experimental techniques, showed that it was possible to control the optical, magnetic, and structural properties of these DMS NCs, confirming the high quality of the synthesized samples.

Therefore, we have proved that the use of glass matrixes, as host material for DMS NCs, is an excellent alternative, since they provide great stability to the nanoparticles, with a relatively low cost of synthesis.

We believe that this chapter may be useful for further investigations on the optical, magnetic, and structural properties of Mn-doped nanocrystals.

8. Acknowledgements

9. References

Archer, P. I.; Santangelo, S. A. & Gamelin, D. R. (2007). Direct Observation of sp-d Exchange Interactions in Colloidal Mn^{2+}- and Co^{2+}-Doped CdSe Quantum Dots. *Nano Lett.*, Vol. 7, Issue 4 (March 2007), pag. 1037, 7 pages, ISSN: 1530-6984

Babentsov, V.; Riegler, J. Scheneider, J.; Ehlert, O.; Nann, T. & Fiederle, M. (2005). Deep level defect luminescence in cadmium selenide nano-crystals films. *J. Cryst. Growth*, Vol. 280, Issue 3-4 (July 2005), pag. 502, 7 pages, ISSN: 0022-0248

Bányai, L. & Koch, S. W. (1993). *Semiconductor Quantum Dots*, World Scientific Publishing Co. Pte. Ltd., ISBN: 9810213905, Singapore

Barbosa, L. C.; Reynoso, V. C. S; de Paula, A. M.; de Oliveira, C. R. M.; Alves, O. L.; Craievich, A. F.; Marotti, R. E.; Brito Cruz, C. H. & Cesar, C. L. (1997). CdTe quantum dots by melting heat treatement in borosilacate glasses. *J. Non-Cryst. Sol.*, Vol. 219, Issue 1 (October 1997), pag. 205, 7 pages, ISSN: 0022-3093

Beaulac, R.; Archer, P. I.; van Rijssel, J.; Meijerink, A. & Gamelin, D. R. (2008). Exciton Storage by Mn^{2+} in Colloidal Mn^{2+}-Doped CdSe Quantum Dots. *Nano Lett.*, Vol. 8, Issue 9 (August 2008), pag. 2949, 5 pages, ISSN: 1530-6984

Bacher, G.; Schömig, H.; Scheibner, M.; Forchel, A.; Maksimov, A. A.; Chernenko, A. V.; Dorozhkin, P. S.; Kulakovskii, V. D.; Kennedy, T. & Keinecke T. L. (2005). Spin-spin interactions in magnetic semiconductor quantum dots. *Physica E*, Vol. 26, Issue 1-4 (February 2005), pag. 37, pages, ISSN: 1386-9477

Becker, R. & Döring, W. (2006). Kinetische Behandlung der Keimbildung in übersättigten Dämpfen. *Ann. Phys.*, Vol. 416 (reprinted from Vol. 24 (1935)), Issue 8 (March 2006), pag. 719, 34 pages, ISSN: 0003-4916

Brus, L. E. (1984). Electron-electron and electron-hole interactions in small semiconductor crystallites: The size dependence of the lowest excited electronic state. *J. Chem. Phys.*, Vol. 80, Issue 9 (May 1984), pag. 4403, 7 pages, ISSN: 0021-9606

Cheng, Y; Wang, Y.; Bao, F. & Chen, D. (2006). Shape Control of Monodisperse CdS Nanocrystals: Hexagon and Pyramid. *J. Phys. Chem. B*, Vol. 110, Issue 19 (April 2006), pag. 9448, 4 pages, ISSN: 1089-5647

Christian, J. W. (1965). *The theory of Transformation in Metal and Alloy*, Pergamon Press, ISBN: 0080440193, Oxford

Dalpian, G. M. & Chelikowsky, J. R. (2006). Self-Purification in Semiconductor Nanocrystals. *Phys. Rev. Lett.*, Vol 96, Issue 22 (June 2006), pag. 226802, 4 pages, ISSN: 0031-9007

Dantas, N. O.; Neto, E. S. F.; Silva, R. S.; Jesus, D. R. & Pelegrini, F. (2008). Evidence of $Cd_{1-x}Mn_xS$ nanocrystal growth in a glass matrix by the fusion method. *Appl. Phys. Lett.*, Vol. 93, Issue 19 (November 2008), pag. 193115, 3 pages, ISSN: 0003-6951

Dantas, N. O.; Silva, R. S.; Pelegrini, F. & Marques, G. E. (2009). Morphology in semimagnetic $Pb_{1-x}Mn_xSe$ nanocrystals: Thermal annealing effects. *Appl. Phys. Lett.*, Vol. 94, Issue 26 (June 2009), pag. 263103, 3 pages, ISSN: 0003-6951

Erwin, S. C.; Zu, L.; Haftel, M. I.; Efros, A. L., Kennedy, T. A. & Norris, D. J. (2005). Doping semiconductor nanocrystals. *Nature*, Vol. 436, Issue 7047 (July 2005), pag. 91, 4 pages, ISSN: 0028-0836

Furdyna, J. K. (1988). Diluted magnetic semiconductors. *J. Appl. Phys.*, Vol. 64, Issue 4 (August 1988), pag. R29, 36 pages, ISSN: 0021-8979

Gaponenko, S. V. (1998). *Optical Properties of Semiconductor Nanocrystals*, Cambridge University Press, ISBN: 0521582415, Cambridge

Hinckley, C. C. & Morgan, L. O. (1965). Electron spin resonance linewidths of mangane (II) ions in concentrated aqueous solutions. *J. Chem. Phys.*, Vol. 44, Issue 3 (1965), pag. 898, 8 pages, ISSN: 0021-9606

Jain, M. K. (1991). *Diluted Magnetic Semiconductors*, World Scientific Publishing Co. Pte. Ltd., ISBN: 9810201761, Singapore

Ji, T.; Jian, W.B.; Fang, J. (2003). The first synthesis of $Pb_{1-x}Mn_xSe$ nanocrystals. *J. Am. Chem. Soc.*, Vol. 125, Issue 28 (June 2003), pag. 8448, 2 pages, ISSN: 0002-7863

Jian, W. B.; Fang, J.; Tianhao, J. & He, J. (2003). Quantum-size-effect-enhanced dynamic interactions among doped spins in $Cd_{1-x}Mn_xSe$ nanocrystals. *Appl. Phys. Lett.*, Vol. 83, Issue 16 (October 2003), pag. 3377, 3 pages, ISSN: 0003-6951

Lee, S.; Dobrowolska, M. & Furdyna, J. K. (2005). Effect of spin-dependent Mn^{2+} internal transitions in $CdSe/Zn_{1-x}Mn_xSe$ magnetic semiconductor quantum dot systems *Phys. Rev. B*, Vol. 72, Issue 7 (2005), pag. 075320, 5 pages, ISSN: 1098-0121

Mukherjee, S.; Pal, A. K.; Bhattacharya, S. & Raittila, J. (2006). Magnetism of Mn_2O_3 nanocrystals dispersed in a silica matrix: Size effects and phase transformations. *Phys. Rev. B*, Vol. 74, Issue 10 (September 2006), pag. 104413, 10 pages, ISSN: 1098-0121

Norris, D. J.; Efros, A. L. & Erwin, S. C. (2008). Doped Nanocrystals. *Science*, Vol. 319, Issue 5871 (March 2008), pag. 1776, 4 pages, ISSN: 0036-8075

Ohno, H. (1998). Making Nonmagnetic Semiconductors Ferromagnetic. *Science*, Vol. 281, Issue 5379 (1998), pag. 951, 6 pages, ISSN: 0036-8075

Sapega, V. F.; Moreno, M.; Ramsteiner, M.; Däweritz, L. & Ploog, K. (2002). Electronic structure of Mn ions in (Ga,Mn)As diluted magnetic semiconductor. *Phys. Rev. B,* Vol. 66, Issue 7 (2002), pag. 075217, 6 pages, ISSN: 1098-0121

Silva, R. S.; Morais, P. C.; Fanyao, Q.; Alcalde, A. M.; Dantas, N. O. & Sullasi, H. S. L. (2007). Synthesis process controlled magnetic properties of $Pb_{1-x}Mn_xS$ nanocrystals. *Appl. Phys. Lett.*, Vol. 90, Issue 25 (June 2007), pag. 253114, 3 pages, ISSN: 0003-6951

Silva, R. S. (2008). *Síntese e Estudo das Propriedades Ópticas e Magnéticas de Pontos Quânticos de $Pb_{1-x}Mn_xS$ Crescidos em Matrizes Vítreas*, Tese (Doutorado em Física)-Universidade de Brasília, 98, [21]f., Brasília

Smyntyna, V.; Skobeeva, V. & Malushin, N. (2007). The nature of emission centers in CdS nanocrystals *Radiation Measurements*, Vol. 42, Issue 4-5 (2007), pag. 693, 4 pages, ISSN: 1350-4487

Volmer, M. & Weber, A. (1926). Nucleus formation in Supersaturated Systems. *Z. Phys. Chem.*, Vol. 119, Issue (1926), pag. 277, 25 pages, ISSN: 0942-9352

Woggon, U. (1997). *Optical Properties of Semiconductor Quantum Dots*, Springer – Verlag, ISBN: 3540609067, Berlin

Xue, H. T. & Zhao, P. Q. (2009). Synthesis and magnetic properties from Mn-doped CdS/SiO_2 core-shell nanocrystals. *J. Phys. D: Appl. Phys.*, Vol. 42, Issue 1 (January 2009), pag. 015402, 5 pages, ISSN: 0022-3727

Zarzycki, J. (1991). *Glasses and the vitreous state*, Cambridge University Press, ISBN: 0521355826, Cambridge

Zhou, H.; Hofmann, D. M.; Alves, H. R. & Meyer, B. K. (2006). Correlation of Mn local structure and photoluminescence from CdS:Mn nanoparticles. *J. Appl. Phys.*, Vol. 99, Issue 10 (May 2006), pag. 103502, 4 pages, ISSN: 0021-8979
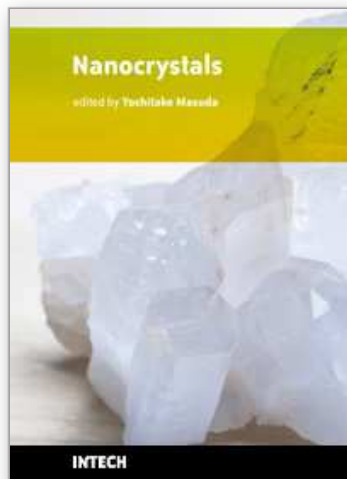
Nanocrystals

Edited by Yoshitake Masuda

This book contains a number of latest research developments on nanocrystals. It is a promising new research area that has received a lot of attention in recent years. Here you will find interesting reports on cutting-edge science and technology related to synthesis, morphology control, self-assembly and application of nanocrystals. I hope that the book will lead to systematization of nanocrystal science, creation of new nanocrystal research field and further promotion of nanocrystal technology for the bright future of our children.

How to reference

In order to correctly reference this scholarly work, feel free to copy and paste the following:

INTECH
open science | open minds